

Raising the Working Temperature of a Triboelectric Nanogenerator by Quenching down Electron Thermionic Emission in Contact-Electrification

Cheng Xu, Aurelia Chi Wang, Haiyang Zou, Binbin Zhang, Chunli Zhang, Yunlong Zi, Lun Pan, Peihong Wang, Peizhong Feng, Zhiqun Lin, and Zhong Lin Wang*

As previously demonstrated, contact-electrification (CE) is strongly dependent on temperature, however the highest temperature in which a triboelectric nanogenerator (TENG) can still function is unknown. Here, by designing and preparing a rotating free-standing mode Ti/SiO₂ TENG, the relationship between CE and temperature is revealed. It is found that the dominant deterring factor of CE at high temperatures is the electron thermionic emission. Although it is normally difficult for CE to occur at temperatures higher than 583 K, the working temperature of the rotating TENG can be raised to 673 K when thermionic emission is prevented by direct physical contact of the two materials via preannealing. The surface states model is proposed for explaining the experimental phenomenon. Moreover, the developed electron cloud-potential well model accounts for the CE mechanism with temperature effects for all types of materials. The model indicates that besides thermionic emission of electrons, the atomic thermal vibration also influences CE. This study is fundamentally important for understanding triboelectrification, which will impact the design and improve the TENG for practical applications in a high temperature environment.

Contact-electrification (CE) (or triboelectrification) is usually deemed as a negative effect because it can cause electrical discharge.^[1,2] However, this phenomenon has been proven useful for many applications such as painting and particle separation.^[3,4] In particular, the newly developed triboelectric nanogenerator (TENG) exhibits an infinitely bright future as a promising technology by harvesting broader-range energy sources in the ambient environment, operating under Maxwell's displacement current.^[5–7] Nearly all of mechanical energies, especially low-frequency energies including water waves,^[8,9] human body motions,^[10,11] and vibrations,^[12–14] can be transformed to electricity through the TENG. Moreover, the energy harvested by the TENG from various sources is an ideal and sustainable energy to power the new era of Internet of Things.^[15]

It is believed that CE always occurs at around room temperature and nearly all conventional TENGs operate in this temperature range.

However, the intriguing question stands: can CE pertain at high temperatures? Present studies of the temperature effect on CE or the TENG are still rare, and there are limited reports that address this question.^[16,17] Wen et al. studied the influence of temperature on the TENG and confirmed its successful operation at the high temperature of 500 K, despite a significant decrease in voltage.^[18] Lu et al. reported that the decrease of the TENG output at high temperatures might be due to the thermal change of the chemical groups and the generation of structural defects on the tribomaterial surface.^[19] However, due to the limitation that TENGs are normally made of conventional polymers,^[20–22] until now the potential occurrence and working mechanism of CE at higher than 500 K have not been elucidated. Our recent study developed a polymer-free TENG that withstood and operated at the temperatures as high as 673 K, providing the possibility to reveal the CE mechanism under high temperatures and develop an unique high-temperature resistant TENG.^[23]

In this paper, Ti/SiO₂ TENGs of different working modes were compared, and finally the rotating free-standing mode TENG was adopted for the study. Through optimizing the device structure, this rotating TENG with double supports produced the greatest

Dr. C. Xu, A. C. Wang, H. Zou, B. Zhang, Dr. C. Zhang, Dr. Y. Zi,
Dr. L. Pan, Dr. P. Wang, Prof. Z. Lin, Prof. Z. L. Wang
School of Materials Science and Engineering
Georgia Institute of Technology
Atlanta, GA 30332-0245, USA
E-mail: zhong.wang@mse.gatech.edu

Dr. C. Xu, Prof. P. Feng
School of Materials Science and Engineering
China University of Mining and Technology
Xuzhou 221116, China

Prof. Z. L. Wang
Beijing Institute of Nanoenergy and Nanosystems
Chinese Academy of Sciences
Beijing 100083, China

Prof. Z. L. Wang
School of Nanoscience and Technology
University of Chinese Academy of Sciences
Beijing 100049, China



The ORCID identification number(s) for the author(s) of this article can be found under <https://doi.org/10.1002/adma.201803968>.

DOI: 10.1002/adma.201803968

output at 523 K. It was revealed that the dominant deterring factor of CE at high temperatures was electron thermionic emission. By further alternating materials and applying preannealing, thermionic emission was prevented and the working temperature of the rotating TENG was risen up to 673 K. The surface states model and the electron cloud-potential well model were then proposed, respectively. These models accounted for the CE mechanism with temperature effects involving metals, dielectrics and polymers, and could be extended to all types of materials.

To realize high temperature resistance, a SiO_2 plate was utilized as the tribomaterial to replace the traditional polymer film and Ti foil rather than Cu foil or Al foil was used as the counter electrode. Figure S1 in the Supporting Information shows the prepared contact-separation mode TENG (C-TENG). The V_{OC} of the C-TENG is only around 1.3 V, similar to the rather small I_{SC} and Q_{SC} . The working principle of the C-TENG is shown in Figure S2 in the Supporting Information. The same size SiO_2 plate and Ti foil from the C-TENG are adopted in the sliding mode TENG (S-TENG) with an equal effective working area. The prepared S-TENG and its working principle are shown in Figures S3 and S4 in the Supporting Information. The S-TENG generates over 15 V of V_{OC} with about 0.1 μA of I_{SC} and 6 nC of Q_{SC} . The fact that the output of S-TENG is much higher than that of C-TENG is attributed to the surface stiffness and roughness of SiO_2 plate. It makes the contact-separation mode difficult to realize perfect contact but creates more opportunities for the sliding mode to contact as much as possible between the SiO_2 plate and Ti foil. This increase of contact area leads to the S-TENG's higher output of V_{OC} , I_{SC} , and Q_{SC} .

Based on the aforementioned results, a rotating free-standing mode TENG (R-TENG) was prepared after making

further improvements (Figure 1a). The R-TENG utilizes a SiO_2 tube whose thickness is the same as that of the SiO_2 plate. The inset in Figure 1a is an optical photograph of the R-TENG. Figure 1b,d is the optical photographs of the SiO_2 tube and Ti foil, respectively. Figure 1c,e is scanning electron microscopy (SEM) image of the surfaces of the SiO_2 tube and Ti foil, respectively. The surface of SiO_2 is smooth while that of the Ti foil has a rough raised texture. These two materials rub against each other through rotation to yield triboelectricity output. The working principle of the R-TENG can be described by the coupling of CE and electrostatic induction. Here, a pair of rotation units including Ti foil and SiO_2 with a back Au electrode is selected to illustrate the process of electricity generation (Figure 1f). Upon contact between SiO_2 and Ti foil, electrons are transferred from Ti foil onto the surface of SiO_2 . Since the two rotation surfaces are completely aligned, triboelectric charges with opposite polarities are fully balanced out, resulting in no electron flow in the external circuit. Once a relative rotation occurs, triboelectric charges on the mismatched areas cannot be compensated. The negative charges on the SiO_2 surface will drive free electrons from one back electrode to the other through the external circuit. The flow of the induced electrons lasts until Ti foil completely matches with the next SiO_2 division with a back Au electrode. As the relative rotation continues, Ti foil starts to leave the second SiO_2 division with a back Au electrode. Thus, the induced electrons will flow back in the opposite direction until the fully aligned position is restored. As shown in Figure 1g,h, the V_{OC} and I_{SC} generated from the R-TENG at room temperature reach 15 V and 0.2 μA , respectively.

Figure 2a is the schematic illustration of the Ti foil and SiO_2 tube layout of the R-TENG. Figure 2b–d is the V_{OC} , I_{SC} , and

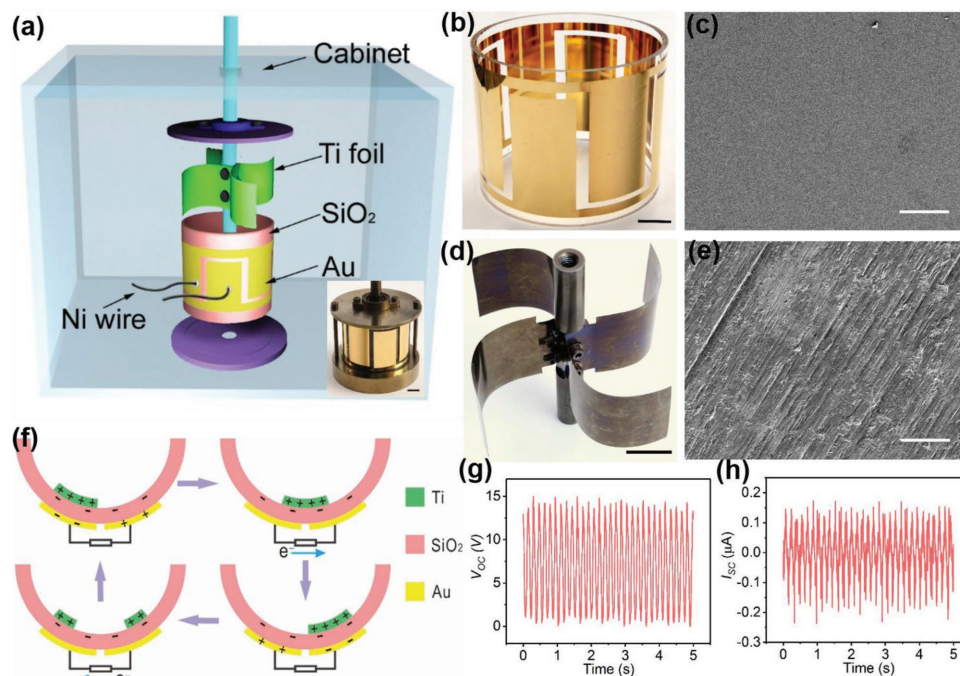


Figure 1. Performance of the R-TENG at room temperature. a) Schematic illustration the R-TENG in the high-temperature measurement platform. Inset is an optical photograph of the R-TENG. b,c) Optical photograph and SEM image of SiO_2 tube. d,e) Optical photograph and SEM image of Ti foil. The black scale bar and white scale bar are 2 cm and 100 μm , respectively. f) The working principle of the R-TENG. g–h) V_{OC} and I_{SC} of the R-TENG at room temperature.

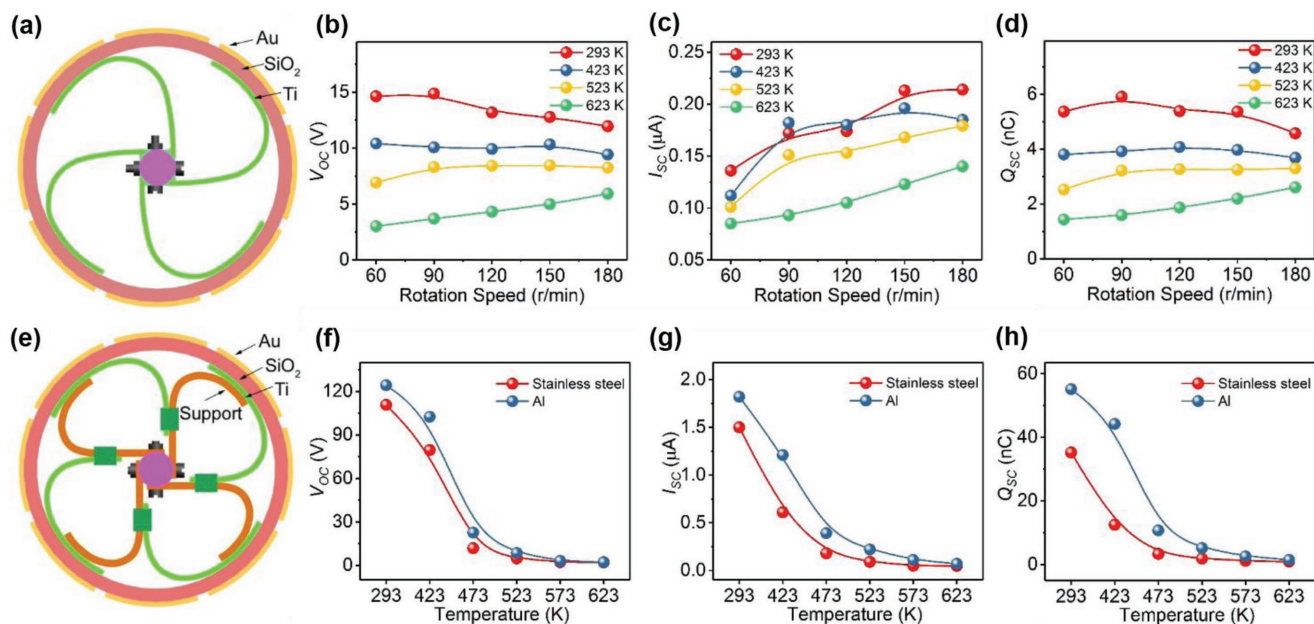


Figure 2. Effect of rotation speed and support material on the R-TENG at different temperatures. a) Schematic illustration of Ti foil and SiO_2 tube of the R-TENG. b–d) V_{OC} , I_{SC} , and Q_{SC} at different rotation rates and temperatures. e) Schematic illustration of the R-TENG with a support. f–h) V_{OC} , I_{SC} , and Q_{SC} of the R-TENG with different supports at different temperatures.

Q_{SC} of the R-TENG at different rotation rates and temperatures. When the speed increases from 60 to 180 r min^{-1} , V_{OC} at room temperature stays constant at first and then slightly declines, while the current gradually increases. For the TENG operated at room temperature, according to our previous work, the amplitudes of V_{OC} and I_{SC} can be represented as:^[24,25]

$$V_{OC} = \frac{Q_{SC}}{C} = \frac{\sigma S}{C} \quad (1)$$

$$I_{SC} = \frac{n \sigma}{\pi 2} S \omega \quad (2)$$

where σ is the triboelectric charge density on the SiO_2 surface, S is the area of one electrode, C is the capacitance between the two electrodes, n is the number of segments on the rotator, and ω is the rotational angular velocity. Referring to Equations (1) and (2), by increasing the rotation speed, the amplitude of V_{OC} and Q_{SC} will keep nearly constant; in the meanwhile, I_{SC} will increase proportionally. When the speed increases to 120 r min^{-1} , the slight decrease of V_{OC} and Q_{SC} may be due to the heating effect, which coincides with the results from increasing the working temperature as follows. With the temperature increase, Figure 2b–d also demonstrates some intriguing phenomena. One is that V_{OC} , I_{SC} , and Q_{SC} all decline with the increase of the temperature. The other is, different from what happens at room temperature, V_{OC} and Q_{SC} gradually rise with the increase of the rotation rate. Both of the above phenomena can be attributed to the electron thermionic emission:^[26,27]

$$J = \lambda A_0 T^2 e^{\frac{W}{kT}} \left[e^{\frac{\Delta W}{kT}} - 1 \right] \quad (3)$$

where J is the thermionic emission current density, λ is the material-specific correction factor, A_0 is the Richardson constant of a free electron, T is the temperature, W is the height of the potential barrier, k is the Boltzmann constant, and ΔW is the potential barrier height variation due to the surface electric field. From Equation (3), it shows that J increases with the increase of temperature, which leads to the decrease of σ on the SiO_2 surface and thus results in the decline of V_{OC} , I_{SC} , and Q_{SC} . Meanwhile, since the CE mechanism replenishes the surface charge of SiO_2 during contact, the increase of the rotation rate will prevent the charge loss and inhibit the thermionic emission, resulting in the rise of V_{OC} and Q_{SC} to some extent. Here, to avoid the disadvantages of the heating effect, all the rotation rates of the R-TENGs are kept at 90 r min^{-1} afterward. In addition, previous studies showed that CE was also influenced by the humidity.^[28–31] For example, Nguyen and Yang demonstrated that there were less charges being transferred at higher moisture level.^[32] Normally the increase of temperature will decrease the relative humidity, which is beneficial to the charge accumulation. At the same time, the increase of temperature will increase the charge loss due to the thermionic emission. These two factors compete with each other, resulting in a complicated trend of the transferred charges in CE. Nevertheless, once the temperature exceeds 373 K (the boiling point of water), the influence of relative humidity can be ignored.

Since the V_{OC} in Figure 2b is only around 15 V, a compound R-TENG with a support is further constructed to realize a V_{OC} improvement (Figure 2e). As shown in Figure 2f–h, V_{OC} , I_{SC} , and Q_{SC} increase at room temperature when using either stainless steel or Al as the support. For instance, the V_{OC} reaches 110 V with stainless steel as the R-TENG support whereas a higher V_{OC} of over 120 V and nearly 2 μA of I_{SC}

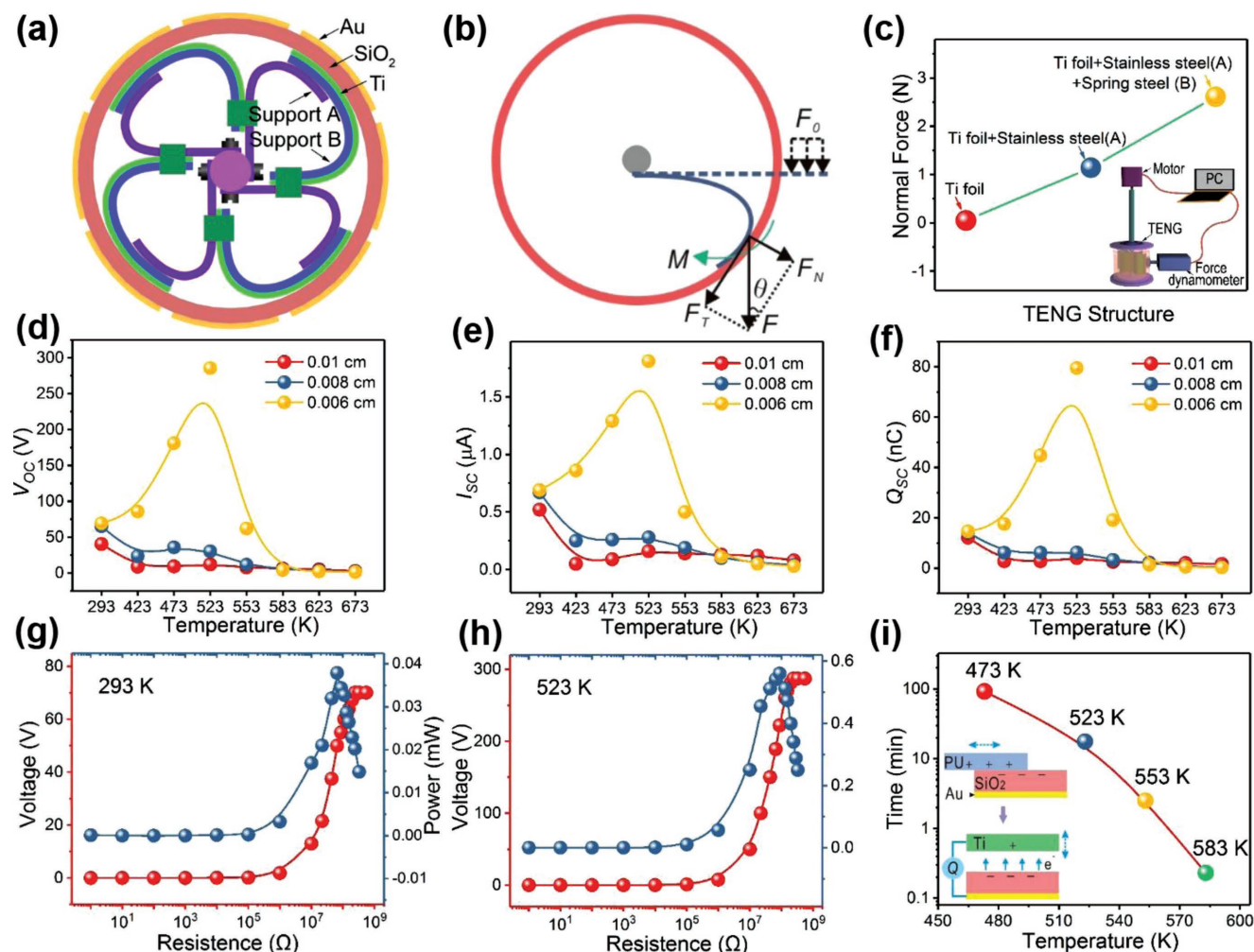


Figure 3. Performance of the R-TENG with double supports at different temperatures. a) Schematic illustration of the R-TENG with double supports. b) Simplified mechanical model of the R-TENG structure. c) Set up of the force measurement platform and the experimental results of F_N . d–f) V_{OC} , I_{SC} , and Q_{SC} of the R-TENG with spring steel (support A) of different thickness under different temperatures. g, h) Dependence of the output power of the R-TENG on resistive loads at 293 and 523 K. i) Procedure of the thermionic emission time measurement and the experimental results at different temperatures.

and 60 nC of Q_{SC} are obtained with Al as the support. This is attributed to the fact that the support increases the friction between the Ti foil and SiO₂ surface. Even though a higher output can be obtained by the R-TENG with a support at room temperature, V_{OC} , I_{SC} , and Q_{SC} still decrease with the increase of temperature.

Figure 3a is the R-TENG constructed with double supports, which is expected to obtain more interaction force between the Ti foil and SiO₂ tube. A simplified mechanic model is constructed in Figure 3b to make a theoretical static analysis of the R-TENG structure. Here, the Ti foil of the R-TENG is regarded as a straight beam. In order to place the Ti foil in the SiO₂ tube, we fixed it at the center of the tube and then bent it by applying a force F_0 at the free end. This process is equivalent to the deformation of a straight beam subjected to external force. The deflection curve of the deformed configuration can be written as a function of $y(x)$. With the help of the Euler–Bernoulli nonlinear beam theory, the bending moment $M(x)$ of the beam at point x can be evaluated with the formula:^[33]

$$M(x) = -E(T)Ip(x) \quad (4)$$

Here, $\rho(x) = \frac{d^2y}{dx^2} \left[1 + \left(\frac{dy}{dx} \right)^2 \right]^{-3/2}$ is the curvature of the deflec-

tion of the beam at point x . $E(T)$ is the Young's modulus, which is constant along the beam, and is a function of temperature T . E decreases in approximate linearity with the increase of T . I is the cross-sectional moment of inertia. For a rectangular cross-section beam with thickness h and width b , $I = \frac{1}{12}bh^3$. EI is the bending stiffness of the beam. For a given initial deformation, the bending moment M linearly depends on the bending stiffness of EI . As a result of the equilibrium condition of the beam, the bending moment $M(A)$ equates $F_T R$ at the contact point A between Ti foil and SiO₂ tube. F_T is the tangential force. R is the radius. The normal force F_N equates $F_T \tan \theta$. Thus, we can obtain the normal force:

$$F_N = -\frac{EI\rho(A)}{R} \tan \theta \quad (5)$$

Here, the value of $\frac{\rho(A)}{R} \tan \theta$ depends on the initial geometric configuration of the beam, which is denoted as G in our experiments. Hence, the normal force $F_N = -E(T)IG$ is proportional to the effective bending stiffness $EI = \frac{E(T)bh^3}{12}$ of the beam. For the R-TENG without supports in Figure 2a, the effective bending stiffness is $E_1I_1 = \frac{bh^3}{12}E_{Ti}(T)$, where E_{Ti} is Young's modulus of Ti foil. Therefore, the normal force without support (F_{N1}) is:

$$F_{N1} = \frac{E_{Ti}(T)bh^3}{12}G \quad (6)$$

For the R-TENG with a support in Figure 2e, both Ti foil and the support can be regarded as cantilever beams which are pre-assembled together. For simplification, we assume that the two beams have the same cross-sections, and their Young's moduli are E_{Ti} and E_s , respectively. Therefore, the normal force with a support (F_{N2}) is:

$$F_{N2} = \frac{bh^3G}{12}[E_{Ti}(T) + E_s(T)] \quad (7)$$

For the R-TENG with double supports in Figure 3a, the effective bending stiffness of the two-layered beam (Ti foil and support B) is $\frac{E_{Ti}(T) + E_B(T)}{3}bh^3$, where E_B is Young's modulus of the support B. The total normal force with double supports (F_{N3}) is:

$$F_{N3} = \frac{bh^3G}{12}[4E_{Ti}(T) + 4E_B(T) + E_A(T)] \quad (8)$$

where E_A is Young's modulus of the support A. If the beams have the same initial geometric configurations, we have a relation of $F_{N1} < F_{N2} < F_{N3}$. Aside from the biggest force being able to be applied by the R-TENG with double supports, another advantage of this structure is having the most stable mechanical properties at high temperatures due to the increased effective bending stiffness.

For further quantitative study, a customized force measurement platform is set up to conduct a F_N test, as shown in the inset of Figure 3c. Prior to the test, trepanning was performed on the side wall of the SiO_2 tube and the probe of the force dynamometer was placed into the hole to contact the Ti foil. The test results show that the F_N of the R-TENGs without support, with a support, and with double supports are 0.2, 1.2, and 2.8 nN, respectively. The increasing trend coincides with the conclusion drawn from theoretical analysis, demonstrating that the double support structure can improve the contact between Ti foil and SiO_2 tube. Figure 3d–f shows the obtained V_{OC} , I_{SC} , and Q_{SC} of the R-TENG after the variation in thickness of spring steel of support A in a double support structure (support B is the same as that in Figure 2e). Figure S5 in the Supporting Information is F_N generated from different thicknesses of spring steel, which shows that the increase of the thickness of spring steel leads to the linear rise of F_N . However, V_{OC} , I_{SC} , and Q_{SC} in Figure 3d–f

show that the phenomena differ from before. One phenomenon is that the increase of F_N decreases V_{OC} , I_{SC} , and Q_{SC} at room temperature, demonstrating that overimposed force leads to negative effects. Another intriguing phenomenon is that with temperature increase, V_{OC} , I_{SC} , and Q_{SC} present a tendency to rise first and then descend, reaching their maximum values at around 523 K under all three steel thicknesses. Moreover, the V_{OC} of the R-TENG with spring steel thickness of 0.006 cm reaches almost 300 V at 523 K, more than three times its initial 70 V. The rise of temperature pushes the peak power up to nearly 0.6 mW at 523 K from the initial 0.04 mW at room temperature (Figure 3g,h). To further confirm whether this phenomenon occurred due to Ti foil or spring steel, we conducted different measurements under the same conditions with Al foil to replace Ti foil and stainless steel to substitute spring steel respectively and found the same results for V_{OC} (Figure S6, Supporting Information). This indicates that the phenomenon is not caused by the special material but is indeed related to the temperature. The reason behind this is the above proposed electron thermionic emission. To quantitatively explore the thermionic emission effect, we designed the thermionic emission time measurement shown in the inset of Figure 3i. First, a SiO_2 plate coated with an Au electrode was rubbed against polyurethane to be negatively charged with around 50 nC. Next, SiO_2 plate and Ti foil were assembled into the C-TENG in Figure S1 in the Supporting Information to conduct charge tests until Q_{SC} decreased to 0.5 nC. The time used in this process was defined as the thermionic emission time. It should be noted that the measurement is simplified since the curved surface of the SiO_2 tube is replaced by the flat surface of the SiO_2 plate. Figure 3i shows that the time decays in an exponent-like from 473 to 583 K. It is well known that usually one hundredth of a second to several seconds is needed for CE to accumulate charges until balance at room temperature.^[34,35] At higher temperatures, the charge accumulation process also occurs, which competes with the charge loss caused by the thermionic emission. At 523 K, the increase of temperature softens the surface of Ti foil and SiO_2 to some extent, enlarging the contact area, and then accumulates more charges under suitable force. However, the thermionic emission time at such a temperature is more than 10 min, which is insufficient to influence charge accumulation and balance processes, and therefore the R-TENG obtains the highest V_{OC} . When the temperature further increases to 553 K, the time decays to around 2 min and the thermionic emission begins to affect the charge accumulation process, leading to the decline of V_{OC} . When the temperature rises up to 583 K, the thermionic emission time, merely 0.2 min, is too short to realize charge accumulation. At that temperature, V_{OC} quickly declines to below 3 V, and I_{SC} and Q_{SC} dramatically decrease as well.

Although Figure 3 demonstrates the detrimental effect of thermionic emission on CE, it also indicates that the charges are likely to be generated at higher temperatures (>583 K) once the thermionic emission is inhibited. Here, two forms of R-TENG improvements are adopted. One is to choose a Ni alloy and Ti alloy with more stable thermodynamic properties to replace spring steel as support A in Figure 3a, intended for better interaction force at high temperature. Despite a larger F_N (6.5 and 10.3 nN respectively) being obtained at room

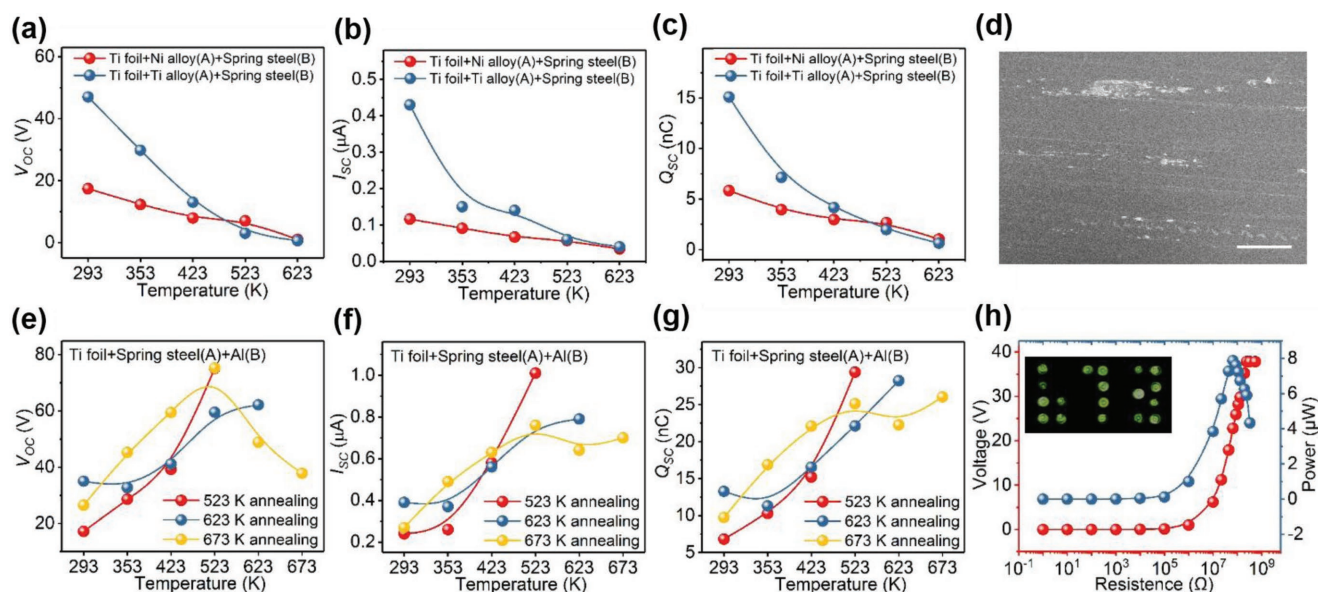


Figure 4. Performance of the double support R-TENGs with different materials and at different annealing temperatures. a–c) V_{OC} , I_{SC} , and Q_{SC} of the R-TENG with Ni alloy and Ti alloy as the support A. d) SEM image of the SiO_2 surface after high temperature measurement. The scale bar is 40 μm . e–g) V_{OC} , I_{SC} , and Q_{SC} of the R-TENG with an Al sheet as support A after different temperature annealing. h) Dependence of the output power of the R-TENG on resistive loads at 673 K. The inset shows that the LEDs can be lit by the R-TENG at 673 K.

temperature, these two alloy-substituted R-TENGs still fail to improve V_{OC} , I_{SC} , and Q_{SC} at more than 523 K (Figure 4a–c). One possible reason is that the larger exerted force causes the inner surface of the SiO_2 tube to be worn down. It is confirmed by SEM image that there are scratches after the high temperature measurement (Figure 4d). The enlarged images show some spalling and even holes on the SiO_2 surface (Figure S7, Supporting Information). Another attempt is to use an Al sheet with low heat resistance rather than spring steel as support A. First, we increased the interaction force between Al sheet and SiO_2 tube to a sufficiently large value (>15 nN) at room temperature. Then, preannealing at different temperatures was performed to the deformed Al sheet and tightly fit SiO_2 tube as close as possible under that temperature. This contact status of the two surfaces will prevent the thermionic emission from SiO_2 surface.^[23] Figure 4e–g shows the obtained V_{OC} , I_{SC} , and Q_{SC} of the R-TENG at different temperatures after preannealing. It is apparent to see that higher V_{OC} , I_{SC} , and Q_{SC} can be obtained once the temperature increases to the annealing temperature, even though those at room temperature are not as high as expected, owing to the thermal expansion and contraction of the Al sheet. For example, after annealing at 623 K, in spite of the mere V_{OC} of less than 40 V at room temperature, over 60 V of V_{OC} can be obtained once the temperature rises up to 623 K. After annealing at 673 K, an interesting phenomenon is that the V_{OC} in Figure 4e increases first and then decreases as the temperature rises. This may be due to that the thermionic emission still plays an important role at the temperature higher than 523 K. Nevertheless, a V_{OC} of nearly 40 V can be obtained at 673 K. Figure 4h demonstrates that the maximum peak power of the R-TENG reaches 8 μW at 673 K. At such high temperature, the R-TENG still manages to light more than ten light emitting diodes (LEDs), which form the numbers of “673” (inset in Figure 4h). However, it should be

noted that under this extreme environment, in addition to abrasion, the properties of materials at high temperature will also change gradually, which may affect the long-term durability of the R-TENG at the same time. This will be explored more in our further study.

According to the experimental results, we propose a CE mechanism between a metal and an insulator dielectric media at high temperatures by using the surface states model. In this model, the electrons in the metal conform to the Fermi–Dirac distribution function.^[36] In the ideal condition, i.e., at absolute zero $T_0 = 0$ K, the electrons will fill up all available energy states below the Fermi level E_F . However, the reality is that the temperature is always above T_0 , and thus some electrons are elevated to the level above the E_F , as shown in Figure 5a following the Fermi–Dirac function. When the metal is in contact with the dielectric (Figure 5b), electrons located at high energy in the metal will transit to the surface states of the dielectric as indicated in process (1), i.e., triboelectrification. When the metal and the dielectric are separated (Figure 5c), the electrons entering into the dielectric surface can also escape because of the thermionic emission effect, i.e., thermionic emission of triboelectric charges, as indicated in process (2). Here, some charges still maintain on the dielectric surface due to its potential barrier, that is, CE occurs. In addition, the electron from the environment may transfer to the metal due to the positive charged surface, as indicated in process (3). Hence, the CE at high temperatures is mainly a competitive outcome of the triboelectrification and thermionic emission of electrons. The higher the temperature is, the more possible the thermionic emission of electrons occur, and the less the net charges remain at the dielectric surface. In any case, the dielectric is negatively charged and the metal is positively charged.

It should be noted that, although the electron transfers from the metal to the dielectric in this study, alternatively, it can also transfer from the dielectric to the metal if the E_n is

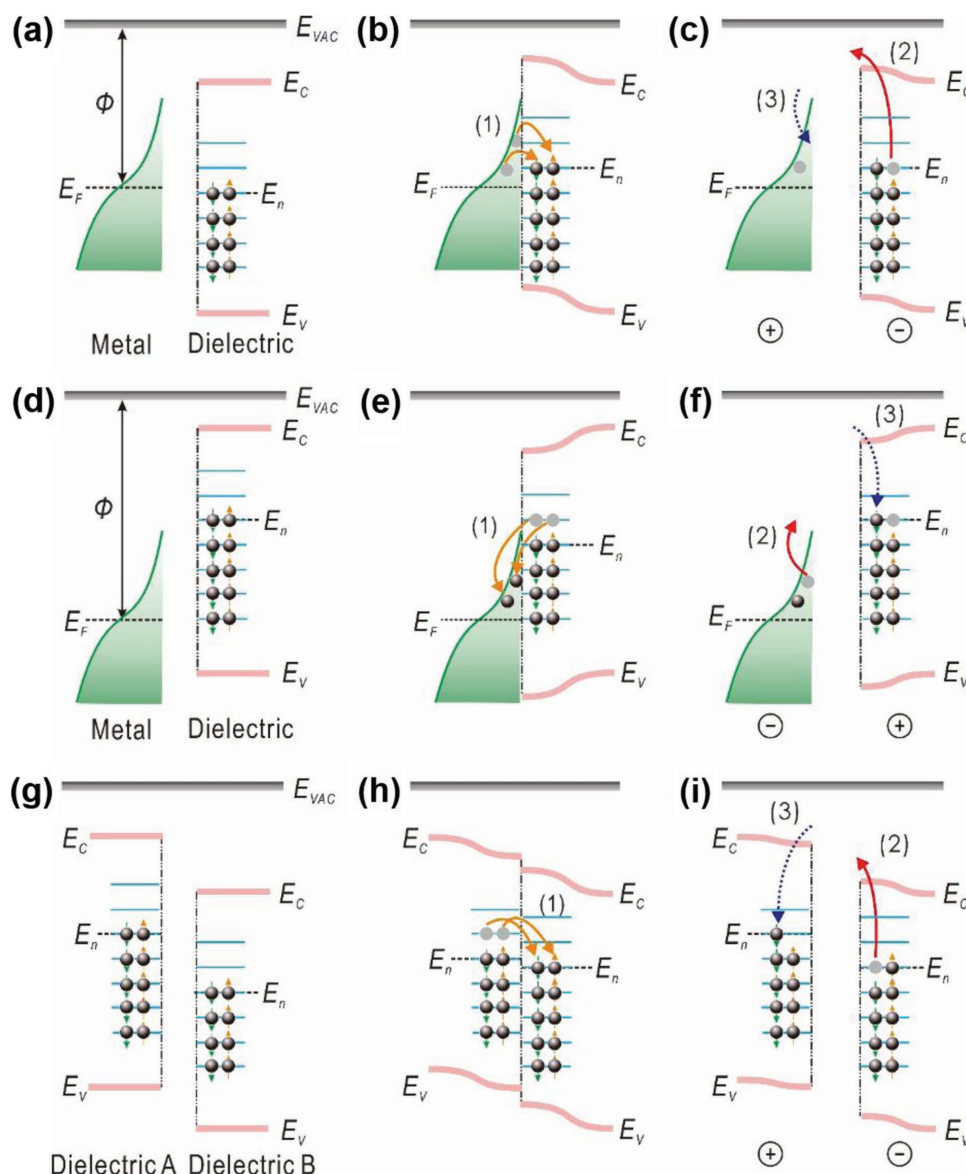


Figure 5. CE mechanism explained by surface states model at high temperatures. a–c) Charge transfer before contact, in contact, and after contact between a metal and an insulator dielectric for a case that E_n is lower than E_F . Φ , metal work function; E_F , Fermi level; E_{VAC} , vacuum level; E_C , conduction band; E_n , neutral level of surface states; E_V , valence band. d–f) Charge transfer before contact, in contact, and after contact between a metal and an insulator dielectric for a case that E_n is higher than E_F . g–i) Charge transfer before contact, in contact, and after contact between two different insulator dielectrics for a case that E_n of the former is higher than that of the later.

higher than the E_F ^[37] as shown in Figure 5d,e. Under this condition, the thermionic emission of triboelectric charges will occur at the metal surface rather than the dielectric surface (process (2) in Figure 5f). In this case, the dielectric is positively charged and the metal is negatively charged. Therefore, there is a possibility of a temperature-induced reversal in the sign of the triboelectric charges on the metal/dielectric surface depending on the interface electronic structure of the metal-dielectric system.

To extend the surface states model, it can be used to account for CE mechanism of two different types of insulator dielectrics at high temperatures. Assume that E_n of dielectric A is higher than that of dielectric B (Figure 5g). When the two dielectrics

contact with each other (Figure 5h), the electron located at high energy states in dielectric A will transit to the low energy states of the surface states of dielectric B, as indicated in process (1). It is similar to the metal-dielectric case in Figure 5b. After the two dielectrics are separated (Figure 5i), the transferred electrons in dielectric B escape from the surface because of thermionic emission, as shown in process (2). Meanwhile, since it currently has more positive charges, dielectric A is likely to capture electrons from the environment as indicated in process (3). Ultimately, dielectric A is positively charged, while dielectric B is negatively charged. It is anticipated that the sign of the transferred charges in this case would not reverse with the increase of temperature.

The previous proposed electron cloud-potential well model^[23] is used to account for the CE mechanism of any two solid materials at high temperatures, such as polymers, cellular, amorphous, or any materials that do not have a well-defined crystal structure. As for these systems, neither band structure nor surface states can be adopted to represent the electronic structure of the materials, but we can start from the atomic or molecular orbits model, which is always the case for a general

material. **Figure 6a** shows that, prior to the atomic contact of the two materials, their respective electron clouds remain separated without overlap. The potential well binds the electrons and stops them from freely escaping, which is the case for non-conducting materials. When the two atoms belonging to two materials, respectively, get close to and contact with each other, the electron clouds overlap between the two atoms to form ionic or covalent bond. The initial single potential wells become an

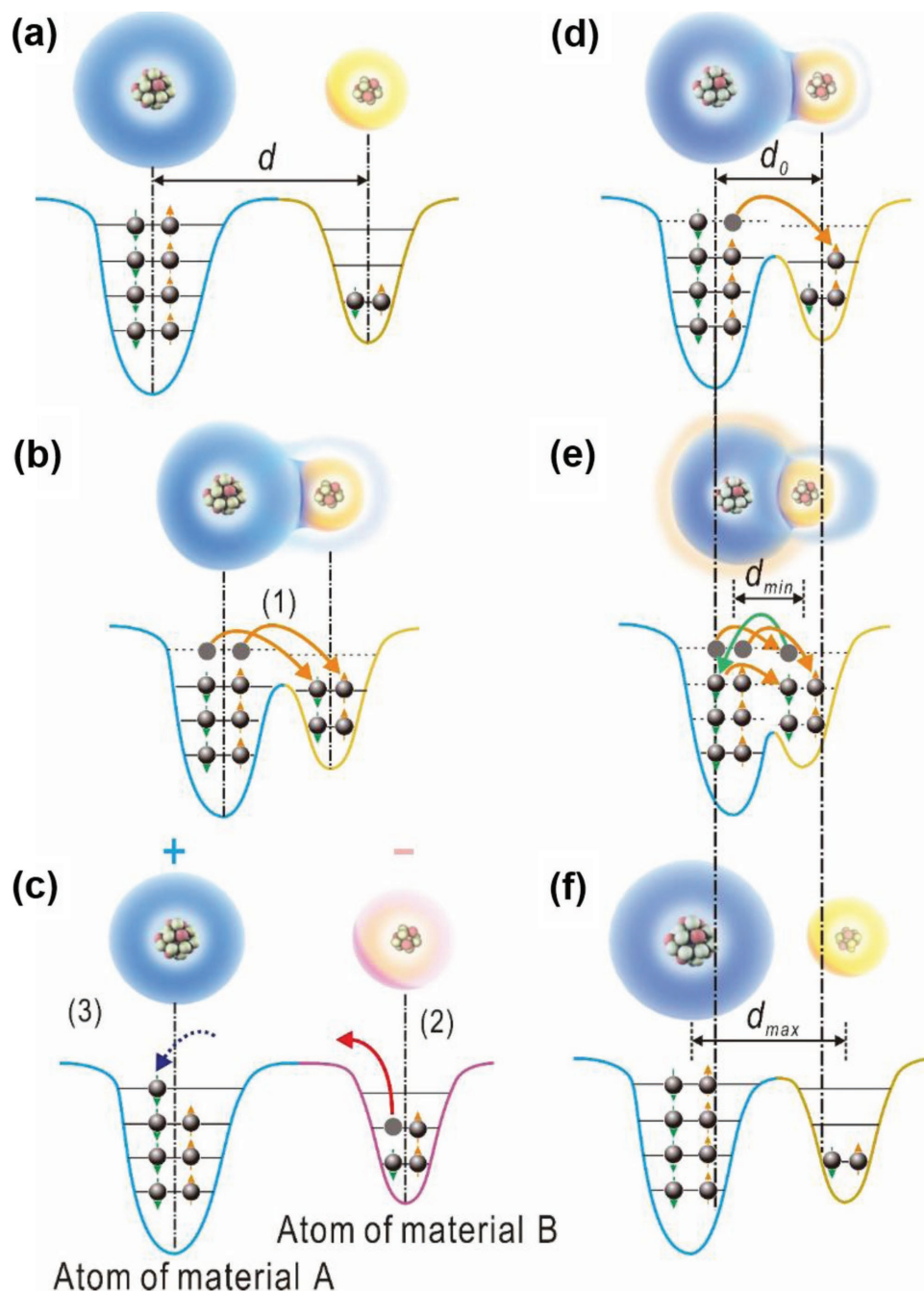


Figure 6. CE mechanism explained by electron cloud-potential well model at high temperatures. a–c) Charge transfer before contact, in contact, and after contact between two atoms of any two solid materials that cannot be simply described by a band structure model. d is the distance between electron clouds of the two atoms belonging to materials A and B, respectively. d–f) Effect of atomic thermal vibration on charge transfer at the distance of d_0 , d_{min} and d_{max} between the two atoms when they are in contact.

asymmetric double-well potential and then electrons can transit from one atom to the other, i.e., triboelectrification, as indicated in process (1) in Figure 6b. The role played by mechanical contacting of the two materials is to shorten the distance between the atoms to cause overlap of their electron clouds, at least at the area at which the atomic-scale contact occurs. This also makes sense that more charges are transferred if one material scrubs the other harder/tighter. After being separated (Figure 6c), the transferred electrons remain, but the thermionic emission of triboelectric charges occurs, resulting in partial release of the electrons from the atom belonging to material B (process (2) in Figure 6c); at the same time, replenishment of electrons from the environment may be taken by the atom of material A (process (3) in Figure 6c), making it less negatively charged.

In practice, the thermionic emitted electrons in processes (2) can be accelerated significantly by the discharging field of the triboelectrification while traveling in vacuum, which can be as high as a few keV in energy. Thus, X-ray emissions can be generated by using the electron exciting a metal target.^[38–40] Light emission is also possible by the thermionic emitted electrons as accelerated by the discharging triboelectric field.

A couple of new light emission processes can be proposed based on the model presented. According to Figures 5g–h, energy released by the electron transfer from dielectric A to dielectric B can be in the form of photon emission. Such characteristic light emission, if possible, can be used for studying the transition from the surface states of dielectric A to the surface states of dielectric B. Secondly, according to Figures 6a–c, light can also be emitted once an electron transit from the shallowed bounded states of atom A to that of the atom B, which belong to two different materials. The emitted photon can be in UV, visible light, microwave and even THz waves. The above proposed processes, if possibly observable as light emission, can give the birth of new spectroscopy for studying electronic transition from one material to the other during CE. These results remain to be verified experimentally.

Based on the conventionally observed surface tribocharge density in air, $\approx 250 \mu\text{C m}^{-2}$,^[41] the charge coverage on a surface is roughly one electron every 10 000 atoms. In other words, for a spherical particle of 20 nm in diameter, the surface has about three triboelectric-induced electrons.

In the models above, we mainly focused on the effect of temperature on the electron transfer during the process of CE. However, besides its influence on the electron distribution and thermionic emission, temperature also affects the positions of the atoms in the material. For a crystalline material, the atomic vibration is well described by phonon models with well-established dispersion relationship. One of the models is the Einstein model in which all of the atoms are vibrating randomly. In this case, we tend to illustrate the effect of atomic thermal vibration on CE when two different atoms do mutual contact by using the electron cloud-potential well model. Figure 6d shows the situation in which the two atoms are in contact with each other. It is, in reality, a nonequilibrium dynamic process due to the atomic thermal vibration around the equilibrium position at high temperature. Suppose the distance between the two atomic nuclei is d , then:

$$d = d_0 + \Delta(T, t) \quad (9)$$

where d_0 is the equilibrium position of the atoms. $\Delta(T, t)$ is the vector difference of the two atoms deviating from the equilibrium position, the function of temperature T and time t . When the two atoms instantaneously separate by d_0 , the electron clouds overlap, the electron with high energy in the atom of material A can transit to the atom of material B, because the transition speed of electrons is much faster than the speed at which the atom vibrates. When the distance between the two atoms instantaneously decreases to the minimum d_{\min} (Figure 6e), the electron clouds overlap the most and the height of the connection place of the corresponding potential wells further decreases. For this case, the electron locates at higher energy in the atom of material A can transit to the atom of material B. Similarly, the electron at higher energy in the atom of material B can also transit to the low energy state in the atom of material A. When the two atoms are instantaneously separated by the maximum distance d_{\max} (Figure 6f), it may well be that the electron clouds of the two atoms remain minimum. In this case, electron transfer does not occur. For all the above mentioned, atomic thermal vibration can influence CE and it is more significant with the temperature increases.

In conclusion, we designed and successfully constructed a R-TENG that worked up to 673 K. We found that the electron thermionic emission played an increasingly more important role for CE with the temperature increase. The surface states model and the electron cloud-potential well model were proposed, revealing that CE at high temperatures was mainly a competitive outcome of triboelectrification and thermionic emission of triboelectric charges. In addition, atomic thermal vibration also influenced CE and it was more significant with the temperature increases. These models contributed to the general CE mechanism with temperature effects for all types of materials. Our study might extend the temperature range of TENG applications to cases such as under diverse extreme environments on planets, in outer space, and even on exoplanets in the solar system.

Experimental Section

Fabrication of the TENG: Ti foil (99.7%) with a thickness of 0.003 cm was purchased from Sigma-Aldrich Co. LLC. A SiO_2 (99%) plate with a thickness of 0.32 cm and a SiO_2 (99%) tube with a diameter of 10 cm and thickness of 0.32 cm were purchased from Technical Glass Products. Spring steel sheets with thicknesses of 0.006, 0.008, and 0.01 cm were purchased from Lyon Industries. Al foil with a thickness of 0.002 cm, stainless steel sheet with a thickness of 0.01 cm, Al sheet with a thickness of 0.02 cm, Ni alloy sheet with a thickness of 0.03 cm, Ti alloy sheet with a thickness of 0.02 cm, and polyurethane foam were purchased from McMaster-Carr. Ti foil and SiO_2 were used as the electrification materials for all of the TENGs. An Au coating with a thickness of 300 nm was deposited on the back of the SiO_2 plate or the outside of the SiO_2 tube as the electrode by using a Denton Explorer E-beam Evaporator. The deposition rate of Au coating was 0.2 nm s^{-1} . After Au deposition, the SiO_2 plate and tube were annealed at 673 K for 4 h in air. The structures of the C-TENG, S-TENG, and R-TENG are shown in Figure S1a,e in the Supporting Information and Figure 1a, respectively. For both the C-TENG and the S-TENG, the maximum effective contact areas between the Ti foil and SiO_2 plate were 21 cm^2 . For the R-TENG, there were eight pieces of Au coating on the outside surface of the SiO_2 tube with two–two piece intervals connected in series to compose two electrodes. The maximum effective contact area between each Ti foil and SiO_2 segment with Au electrode was 19 cm^2 .

Measurement of the TENG: The TENGs were placed in a heating cabinet (Barnstead/Thermolyne 6000 furnace), which provided the desired temperature with an accuracy of ± 5 K. The heating rate of the cabinet was about 7.5 K min^{-1} . For both the C-TENG and the S-TENG, a SiO_2 plate with Au coating was positioned on an insulating ceramic plate, and another ceramic plate was added between the Ti foil and steel holder. The top of the steel holder on the TENG extended out of the heating cabinet and was connected with a linear motor. Nickel wires were attached to the surfaces of the Au electrode and Ti foil and extended out of the heating cabinet. For the R-TENG, the SiO_2 tube was positioned between two stainless steel plates. There was a rotatable stainless-steel rod inside the SiO_2 tube with four pieces of Ti foils fixed on as rotor blades. The top of the steel rod extended out of the open hole on the heating cabinet and was connected with a rotary motor. Nickel wires were attached to the surfaces of each of the two Au electrodes and extended out of the heating cabinet. The environmental relative humidity was less than 30%. During the TENGs' performance measurements, the motor provided an accurate control of position and speed for the mechanical stimulation, and the heating cabinet controlled the temperature. The relative humidity was measured by a Shaw Superdew 3 hygrometer. The open-circuit voltage V_{OC} , short-circuit current I_{SC} , and short-circuit transfer charge Q_{SC} of the TENGs were tested under different temperatures after holding for 15 min by a Keithley 6514 electrometer. The microscope images of Ti foil and SiO_2 were measured by a Hitachi SU8010 field-emission scanning electron microscope (SEM). The normal forces between Ti foil and the SiO_2 tube of the R-TENGs were measured by a Vernier LabQuest Mini force dynamometer.

Supporting Information

Supporting Information is available from the Wiley Online Library or from the author.

Acknowledgements

C.X., A.C.W., H.Z., and B.Z. contributed equally to this work. The authors are grateful for the support received from Hightower Chair foundation, MANA, NIMS (Japan), the National Key R & D Project from Minister of Science and Technology (2016YFA0202704), China, National Natural Science Foundation of China (51432005, 5151101243, and 51561145021). C.X. thanks the Six Talent Peaks Project in Jiangsu Province, China (2015-XCL-009) and the Outstanding Teacher Overseas Research Project of China University of Mining and Technology.

Conflict of Interest

The authors declare no conflict of interest.

Keywords

atomic thermal vibration, contact-electrification, nanogenerators, thermionic emission, triboelectrification

Received: June 22, 2018
Revised: July 23, 2018
Published online:

- [1] N. Gibson, *J. Electrostat.* **1997**, 40–41, 21.
[2] R. D. Lorenz, *Space Sci. Rev.* **2008**, 137, 287.

- [3] F. R. Fan, Z. Q. Tian, Z. L. Wang, *Nano Energy* **2012**, 1, 328.
[4] C. Zhang, W. Tang, C. Han, F. R. Fan, Z. L. Wang, *Adv. Mater.* **2014**, 26, 3580.
[5] Y. Yang, H. Zhang, J. Chen, Q. Jing, Y. S. Zhou, X. Wen, Z. L. Wang, *ACS Nano* **2013**, 7, 7342.
[6] M. Ma, Z. Zhang, Q. Liao, F. Yi, L. Han, G. Zhang, S. Liu, X. Liao, Y. Zhang, *Nano Energy* **2017**, 32, 389.
[7] Z. L. Wang, *Mater. Today* **2017**, 20, 74.
[8] T. Jiang, L. M. Zhang, X. Chen, C. B. Han, W. Tang, C. Zhang, L. Xu, Z. L. Wang, *ACS Nano* **2015**, 9, 12562.
[9] C. Wu, R. Liu, J. Wang, Y. Zi, L. Lin, Z. L. Wang, *Nano Energy* **2017**, 32, 287.
[10] P. Wang, R. Liu, W. Ding, P. Zhang, L. Pan, G. Dai, H. Zou, K. Dong, C. Xu, Z. L. Wang, *Adv. Funct. Mater.* **2018**, 28, 1705808.
[11] H. Zhang, Y. Yang, T.-C. Hou, Y. Su, C. Hu, Z. L. Wang, *Nano Energy* **2013**, 2, 1019.
[12] J. Chen, G. Zhu, W. Yang, Q. Jing, P. Bai, Y. Yang, T. C. Hou, Z. L. Wang, *Adv. Mater.* **2013**, 25, 6094.
[13] J. Yang, J. Chen, Y. Yang, H. Zhang, W. Yang, P. Bai, Y. Su, Z. L. Wang, *Adv. Energy Mater.* **2014**, 4, 1301322.
[14] M.-L. Seol, J.-W. Han, D.-I. Moon, M. Meyyappan, *Nano Energy* **2017**, 39, 238.
[15] Z. L. Wang, T. Jiang, L. Xu, *Nano Energy* **2017**, 39, 9.
[16] Y. Yang, Y. Zhou, J. M. Wu, Z. L. Wang, *ACS Nano* **2012**, 6, 8456.
[17] Z. Zhao, X. Pu, C. Du, L. Li, C. Jiang, W. Hu, Z. L. Wang, *ACS Nano* **2016**, 10, 1780.
[18] X. Wen, Y. Su, Y. Yang, H. Zhang, Z. L. Wang, *Nano Energy* **2014**, 4, 150.
[19] C. X. Lu, C. B. Han, G. Q. Gu, J. Chen, Z. W. Yang, T. Jiang, C. He, Z. L. Wang, *Adv. Energy Mater.* **2017**, 19, 1700275.
[20] Z. L. Wang, *Faraday Discuss.* **2014**, 176, 447.
[21] N. Sun, Z. Wen, F. Zhao, Y. Yang, H. Shao, C. Zhou, Q. Shen, K. Feng, M. Peng, Y. Li, X. Sun, *Nano Energy* **2017**, 38, 210.
[22] Y. Zi, S. Niu, J. Wang, Z. Wen, W. Tang, Z. L. Wang, *Nat. Commun.* **2015**, 6, 8376.
[23] C. Xu, Y. Zi, A. C. Wang, H. Zou, Y. Dai, X. He, P. Wang, Y. Wang, Z. L. Wang, *Adv. Mater.* **2018**, 30, 1706790.
[24] S. Niu, Y. Liu, X. Chen, S. Wang, Y. S. Zhou, L. Lin, Y. Xie, Z. L. Wang, *Nano Energy* **2015**, 12, 760.
[25] L. Lin, S. Wang, Y. Xie, Q. Jing, S. Niu, Y. Hu, Z. L. Wang, *Nano Lett.* **2013**, 13, 2916.
[26] C. Crowell, *Solid-State Electron.* **1965**, 8, 395.
[27] J. Racko, A. Grmanová, J. Breza, *Solid-State Electron.* **1996**, 39, 391.
[28] J. A. Wiles, M. Fialkowski, M. R. Radowski, G. M. Whitesides, B. A. Grzybowski, *J. Phys. Chem. B* **2004**, 108, 20296.
[29] Y.-T. Jao, P.-K. Yang, C.-M. Chiu, Y.-J. Lin, S.-W. Chen, D. Choi, Z.-H. Lin, *Nano Energy* **2018**, 50, 513.
[30] J. Shen, Z. Li, J. Yu, B. Ding, *Nano Energy* **2017**, 40, 282.
[31] K. Y. Lee, J. Chun, J.-H. Lee, K. N. Kim, N.-R. Kang, J.-Y. Kim, M. H. Kim, K.-S. Shin, M. K. Gupta, J. M. Baik, S.-W. Kim, *Adv. Mater.* **2014**, 26, 5037.
[32] V. Nguyen, R. Yang, *Nano Energy* **2013**, 2, 604.
[33] D. G. Fertis, *Nonlinear Structural Engineering*, Springer, Berlin **2006**.
[34] G. A. Cottrell, *J. Phys. D* **1978**, 11, 681.
[35] J. Lowell, A. C. Rose-Innes, *Adv. Phys.* **1980**, 29, 947.
[36] F. Reif, *Fundamentals of Statistical and Thermal Physics*, McGraw-Hill, New York **1965**.
[37] L.-H. Lee, J. Lowell, *J. Electrostat.* **1994**, 32, 1.
[38] C. G. Camara, J. V. Escobar, J. R. Hird, S. J. Putterman, *Nature* **2008**, 455, 1089.
[39] H. Stöcker, M. Rühl, A. Heinrich, E. Mehner, D. C. Meyer, *J. Electrostat.* **2013**, 71, 905.
[40] K. Nakayama, *Tribol. Lett.* **2010**, 37, 215.
[41] J. Wang, S. Li, F. Yi, Y. Zi, J. Lin, X. Wang, Y. Xu, Z. L. Wang, *Nat. Commun.* **2016**, 7, 12744.